


# Robotic Multiple Peg-in-Hole Assembly with Deviation Estimation and Fast Insertion Control

Dianxi Li , Xiangfei Li , *Member, IEEE*, Huan Zhao , *Member, IEEE*, Dongsheng Ge ,  
and Han Ding , *Senior Member, IEEE*

**Abstract**—Due to the large state–action space and statically indeterminate problem, it is difficult to analyze the robotic multiple peg-in-hole (PIH) assembly tasks, which results in a scarcity of effective and general multiple PIH assembly strategies and control methods. This is particularly evident when faced with situations involving a large number of pegs and holes, as well as small fitting clearances. Besides, when the assembly components are visually inaccessible, there is a lack of efficient methods for deviation estimation, compensation, and adjustment. In order to deal with these problems, this study proposes a general three-stage strategy for robotic multiple PIH assembly which can simplify the planning and control methods. In the first stage, the contact state of the peg-hole is passively adjusted, thereby confining deviations within a plane. Building upon this, the second stage introduces a deviation estimation method that relies solely on force/torque information. In addition, a fast and effective control method for the final insertion stage is presented. Experiments are conducted on three sets of components with six or seven peg–hole pairs. The results demonstrate that the proposed strategy offers effective resolution for the complex multiple PIH tasks. Additionally, the deviation estimation method in the second stage has the ability to greatly compensate for the deviation and control the estimation error within an acceptable range. Lastly, the proposed insertion control method can efficiently complete the assembly in the presence of residual deviations caused by the deviation estimation method.

**Index Terms**—Deviation estimation, insertion control, robots, multiple peg-in-hole (PIH) assembly.

## I. INTRODUCTION

**P**EG-IN-HOLE (PIH) assembly is a fundamental process for a wide range of industry manufacturing tasks, such as aviation components assembly [1], microelectromechanical systems assembly [2], and automobile assembly [3]. While robots have been employed to replace humans in certain assembly tasks, their use is mainly confined to structured envi-

ronments [4] and simple single PIH work. However, the actual complex assembly scenarios, where multiple PIH tasks are frequently performed, require the robots to have exceptional operational abilities and be capable of adapting to unstructured environments [5], which still remains a challenging problem for researchers [6].

To execute the multiple PIH tasks in an unstructured environment, the relative posture or contact state between the pegs and holes must first be determined. Then, a strategy needs to be devised to regulate the assembly motion across a large state–action space, which poses significant challenges. This process mainly involves utilizing two types of information: vision and force/torque. Vision measuring technologies, such as laser, RGB, and depth cameras, have been widely used in robotic assembly applications for pose recognition and robotic motion planning [7]. For instance, based on multicamera microscopic vision, Qin et al. [8] established action classes of image features to guide motion in the sleeve–cavity and coil–cylinder assembly tasks. To overcome the robot PIH prealignment problem, a vision system with a new measurement method was proposed by Jiang et al. [9].

Another type of information is force/torque information, based on which relevant methods can be categorized into two types: model-based and learning-based methods. The core of model-based techniques is constructing a contact model and subsequently executing a compliant assembly by utilizing force feedback, which relies on the perception and estimation of the model [10]. For example, Tang et al. [11] proposed a three-point contact model based on which they further estimated the pose deviation between the peg and hole. The force analysis for both rigid and flexible dual PIH assemblies was developed by Zhang et al. [12]. In contrast, learning-based approaches do not necessitate the construction of the contact model. This type of approach mainly includes two categories: imitation learning (IL) and reinforcement learning (RL). The IL approaches such as dynamic motion primitives (DMP) [13], [14], [15], Gaussian mixture model (GMM) [16], and hidden Markov model (HMM) [17], [18] have been widely utilized in single robotic assembly. However, relying solely on assembly skills learned from expert demonstrations is insufficient to address the multiple PIH problems. In contrast, RL approaches offer the capability to adapt and refine these skills through autonomous exploration and interaction with the environment. Consequently, RL approaches have been more widely investigated in the context of the multiple PIH problems. For instance, Hou et al. [19] proposed a

Manuscript received 23 January 2024; revised 11 April 2024; accepted 20 May 2024. Date of publication 27 June 2024; date of current version 12 November 2024. This work was supported by the National Natural Science Foundation of China under Grant 52090054, Grant 52205521, and Grant 52188102. (*Corresponding author: Huan Zhao.*)

The authors are with the State Key Laboratory of Intelligent Manufacturing Equipment and Technology, School of Mechanical Science and Engineering, Huazhong University of Science and Technology (HUST), Wuhan, Hubei 430074, China (e-mail: huanzhao@hust.edu.cn).

Digital Object Identifier 10.1109/TIE.2024.3406860

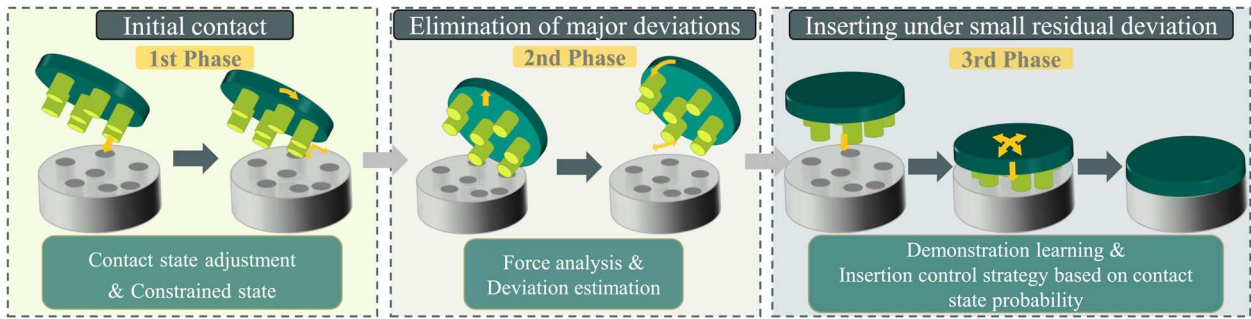


Fig. 1. Overview of the assembly strategy.

learning-based algorithm based on deep deterministic policy gradient (DDPG) to solve a triple PIH problem in simulation and a dual PIH problem in a real-world experiment. Similarly, a model-driven DDPG (MDDDPG) was presented by Xu et al. [20] to solve the dual PIH problem both in simulation and the real world.

However, force-based methods also have several limitations in addressing the multiple PIH problems. Currently, there is a scarcity of efficient and general assembly models available [21], [22], particularly when dealing with more than three pairs of pegs and holes, as the analytical complexity of such models escalates rapidly with an increase in the number of pegs, which means a small number of pegs and holes will lead to a large number of contact states [5], [23]. In addition, it is difficult to identify the contact state based on the current contact force/torque due to the statically indeterminate problem [24]. Due to these reasons, RL and IL methods have not been applied to situations involving more than three pairs of pegs and holes [25]. RL-based methods also need the initial deviations to be small. Moreover, when there are changes in the geometric characteristics, retraining may become necessary for the RL approaches, which not only consumes a substantial amount of time but also poses a potential risk of damage to both the robots and the objects involved [26]. Additionally, different force-based compliant control methods, such as impedance/admittance control (IMC/ADC) and force-position hybrid control [27], also have limitations [28], [29] in the assembly tasks. For instance, IMC/ADC can result in misadjustment of orientation and a long execution time due to oversimplified causality between pose and forces/moments in PIH problems [4], [26]. In response to the aforementioned issues, the first objective of this study is to contribute to the research on assembly strategies and control methods for scenarios involving a large number of pegs and holes.

In [30], the issue of multiple PIH assembly with predetermined pose of holes has been effectively addressed. Nevertheless, the extension of this approach to more unstructured environments, characterized by the unknown relative orientation of pegs and holes, still presents a formidable challenge. Although vision-based techniques may present an effective solution, they face obstacles such as exorbitant expenses, poor performance in small-scale interactions, narrow space, view occlusion, and the complex operating environment [31]. These challenges can impede the efficient recognition of deviations as

well as the avoidance of large assembly strains [32]. Drawing inspiration from the strategies and skills employed by humans in performing multiple PIH assembly tasks, it can be observed that humans can estimate the approximate angular deviations of the holes and adjust the poses through force/torque perception, even when their eyes are closed. Motivated by this human capability, the second objective of this study is to enable robots to exhibit similar aptitude in deviation estimation and insertion, thereby emulating human-like performance.

The specific contributions of this work are outlined as follows: (1) A three-stage progressive deviation-reduction strategy is designed to facilitate the model construction and control within a smaller action-state space at each stage, which reduces deviations until the assembly is completed. (2) Inspired by the human assembly process, a vision-free deviation estimation method is proposed to estimate the deviations solely based on the force/torque information. (3) A fast insertion control method is proposed to efficiently eliminate the residual deviations primarily caused by estimation error. In summary, the proposed strategies and methods in this article not only address the current lack of efficient control methods and strategies for multiple PIH assembly in scenarios with a large number of peg-hole pairs (three or more), but also demonstrate improved adaptability to assembly scenarios where the orientation of the holes is not fixed, compared with existing approaches. The proposed methods were evaluated by conducting challenging multiple PIH assembly experiments with various clearances, materials, and number of pegs and holes, demonstrating that the strategy can effectively resolve complex analysis and control design difficulties associated with multiple PIH tasks.

The remaining parts of this article are organized as follows: Section II first proposes an overview of the strategy for the multiple PIH tasks and then provides detailed analysis for each stage, including the deviation estimation method and insertion control method. Section III tests the performance of the proposed methods through numerous and comparative experiments in the real world. The conclusions are given in Section IV.

## II. MULTIPLE PIH STRATEGY

### A. Overview of Assembly Strategy

Fig. 1 shows the three stages of the proposed robotic multiple PIH assembly strategy. It aims to partially eliminate the

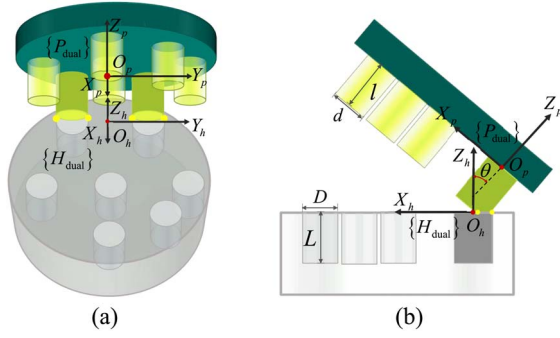


**Fig. 2.** Symmetric, stable, constrained contact state. The contact points are marked in yellow and are symmetrically arranged with respect to the planes  $Z_p O_p X_p$  and  $Z_h O_h X_h$ . The length of the pegs and the holes are  $l$  and  $L$ , while their diameters are  $d$  and  $D$ , respectively. (a) Front upper view. (b) Frames viewed in the plane  $Z_h O_h X_h$ .

system's deviations at each stage, thereby avoiding the difficulties associated with directly planning in a large state–action space. The multipeg component initially moves toward the multihole component and subsequently adjusts to achieve a specific contact state. In the next stage, the angular and positional deviations are estimated based on the contact force/torque, allowing the robot to lift the multipeg component and compensate for the deviation while in the air. Finally, the pegs are inserted into the holes.

### B. Initial Contact State Adjustment and Analysis

The contact conditions in multi PIH assemblies are complex, making it difficult to perform mechanical and geometric analysis [33]. The purpose of the first stage is to tackle this challenge by adjusting the multi-peg and multihole components to a specific contact state.

1) *Contact State Adjustment:* Consider a multipeg–hole system where each peg is rigid and has the same geometric dimensions, but their distribution on the plate is not specified. Since each peg may come into contact with a hole and can correspond to different orientations, it is difficult to classify all contact states through exhaustive enumeration. However, adjusting the components to a specific contact state can facilitate the force and geometric analysis. As the contact state in Fig. 2 shows, the two dark green adjacent pegs make contact with their corresponding holes. The geometric symmetry of the two pegs ensures that all contact points, as well as the associated contact forces and torques, exhibit symmetry with respect to the plane  $X_p O_p Z_p$ .

This symmetrical contact state has the following advantages:

- 1) This state can be easily achieved by passively following the contact forces/torques.
- 2) Due to the symmetry in the contact configuration, the analysis of contact forces and torques can be simplified by projecting them onto the plane  $X_p O_p Z_p$ , reducing the complexity of force analysis.
- 3) The deviations are concentrated within the plane  $X_p O_p Z_p$ , thereby reducing the dimensionality of the

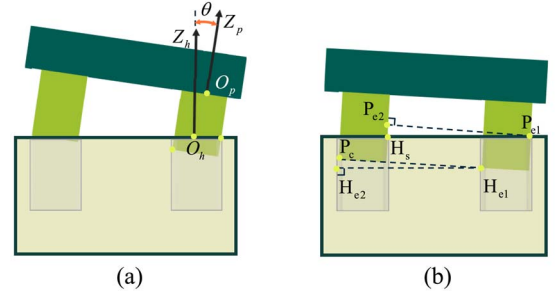


**Fig. 3.** Analysis of the constrained state. This figure shows the projections of the pegs and holes on the plane  $X_p O_p Z_p$ . (a) In the constrained state, when the angle  $\theta$  is less than  $\arccos(d/D)$ , the two pegs fall into the holes, resulting in a two-point contact between them. (b) Under the constrained state, at most one pair of peg and hole can be in contact within the equivalent plane.

parameter space for the design and learning of control methods.

A detailed description of the adjustment method is provided in [30]. The basic idea is that when the contact force surpasses a predefined threshold, the double-peg will move in the direction of the force error and thus mitigate the contact force to stabilize the system. With this control method, the system can eventually adapt to the symmetrical contact state, even if there is a significant initial deviation, such as having only one peg in contact with the hole initially. At the end of this stage, the plane  $X_p O_p Z_p$  coincides with the plane  $X_h O_h Z_h$ , and any remaining deviations outside this plane are eliminated. For convenience, this article refers to this contact state and space as the constrained state and constrained space, respectively, and the  $X_p O_p Z_p$  plane as the equivalent plane.

2) *Contact State Analysis:* The purpose of this part is to prove that under the constraint state, only one pair of pegs and holes is in contact among the multiple peg–hole pairs, which serves as a prerequisite for subsequent force analysis, deviation estimation, and control method design. While Fig. 3 illustrates only two pairs of peg–hole projections on the equivalent plane, it is worth noting that the proof process can be readily extended to any number of peg–hole pairs. As illustrated in Fig. 3(a), if the angle  $\theta$  between the axes  $Z_p$  and  $Z_h$  is less than  $\arccos(d/D)$ , the two pegs will enter the holes and will be in a two-point contact state with the corresponding holes. As shown in Fig. 3(b), the right peg makes contact with the hole at the upper surface points  $P_{e1}$  and  $H_{e1}$ , where  $H_s$  denotes the rightmost point on the upper surface edge of the left hole, and  $P_c$  represents the leftmost point on the lower surface edge of the left peg. Since the distribution of pegs is identical with the distribution of holes, the length of  $P_{e1}P_{e2}$  is equal to the length of  $P_{e1}H_s$  (the distance between pegs and the distance between holes are the same). If  $H_s$  were also a contact point on the left peg, it would imply two right angles in the triangle  $H_sP_{e1}P_{e2}$ , which is obviously impossible. Therefore,  $H_s$  cannot be a contact point on the left peg. Similarly, in the triangle  $H_{e1}H_{e2}P_c$ , we can derive a similar conclusion that  $P_c$  cannot be a contact point either. Therefore, apart from the right peg, all the other pegs do not make contact.



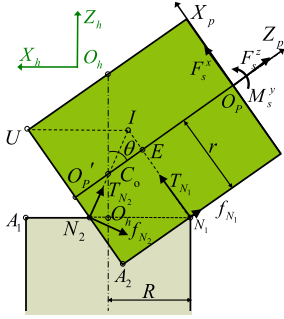


**Fig. 4.** Force and deviation analysis in the equivalent plane  $X_h O_h Z_h$

### C. Force Analysis and Deviation Estimation

In the second stage, deviations outside the plane  $X_p O_p Z_p$  have been eliminated. All angular and positional deviations are concentrated within the plane  $X_p O_p Z_p$  and can be represented as functions of the deviation angle  $\theta$ . Since it has been proven that only one pair of pegs and holes come into contact in the constrained state, it is sufficient to conduct force analysis on this specific pair of pegs and holes. As illustrated in Fig. 4, the point  $O_{p'}$  is the midpoint of the bottom surface of the peg, and the axes of the peg and the hole intersect at point  $C_o$ . The distance from the point  $C_o$  to the points  $O_{p'}$  and  $O_h$  are

$$\begin{aligned} a_1 &= |C_o O_{p'}| = (R - r \cos \theta) / \sin \theta \\ a_2 &= |C_o O_h| = (r - R \cos \theta) / \sin \theta. \end{aligned} \quad (1)$$

The pegs and holes come into contact at points  $N_2$  and  $N_1$ , and the distances from the point  $N_2$  to the points  $O_h$ ,  $O_{p'}$ , and  $C_o$  are, respectively

$$\begin{aligned} k_1 &= |N_2 O_h| = (a_1 - a_2 \cos \theta) / \sin \theta \\ k_2 &= |N_2 O_{p'}| = (a_1 \cos \theta - a_2) / \sin \theta \\ k_3 &= |N_2 C_o| = \sqrt{a_1^2 + k_2^2}. \end{aligned} \quad (2)$$

1) *Force Analysis:* The supporting force  $T_{N_2}$  at the point  $N_2$  is directed toward the point  $C_o$ , while the supporting force  $T_{N_1}$  at the point  $N_1$  is perpendicular to the generatrix of the peg and directed toward point  $E$  on the axis  $Z_p$ , where the length of  $|EO_P|$  is  $2a_1$ . The two frictional forces are perpendicular to their respective supporting forces, and their magnitudes are  $\mu T_{N_1}$  and  $\mu T_{N_2}$ , respectively, where  $\mu$  is the coefficient of friction. All supporting and frictional forces produce resultant forces  $f_s^x$ ,  $f_s^z$ , and torque  $m_s^y$  at the point  $O_p$ , and their relationships are

$$\begin{aligned} f_s^x &= T_{N_2}(-k_2 - \mu a_1)/a_3 + T_{N_1} \\ f_s^z &= T_{N_2}(a_1 + \mu k_2)/a_3 + \mu T_{N_1} \\ f_s^y &= k_2 T_{N_2}(l - a_1)/a_3 - T_{N_1}(l - 2a_1) \\ &\quad - (la_1 + k_2^2)/a_3. \end{aligned} \quad (3)$$

Substituting (1) and (2) into (3) and solving them simultaneously yields

$$\begin{aligned}
T_{N_1} &= (a_1 f_s^x + k_2 f_s^z + \mu f_s^z a_1 + \mu f_s^x k_2) / b_1 \\
T_{N_2} &= a_3 (f_s^z - \mu f_s^x) / b_1 \\
m_s^y &= \left[ f_s^x (2b_3^2 + \frac{\mu^2 b_2^2}{(\sin\theta)^2} - lb_3 \sin\theta - \frac{3\mu b_3 b_2}{\sin\theta} \right. \\
&\quad + \mu \sin\theta r b_3 + 2\mu l b_2 + \mu^2 l b_3 \sin\theta - \mu^2 l r b_2) + f_s^z (2\mu b_3^2 \\
&\quad - \frac{\mu b_2^2}{(\sin\theta)^2} - \frac{b_2 b_3}{\sin\theta} - 2\mu l b_3 \sin\theta - 2\mu l b_3 \sin\theta - \mu r b_2 \\
&\quad \left. + \mu^2 r b_3 \sin\theta) \right] / (b_3 \sin\theta - 2\mu b_2 + \mu^2 b_3) \quad (4)
\end{aligned}$$

where

$$\begin{aligned} b_1 &= \mu^2 a_1 + 2\mu k_2 + a_1 \\ b_2 &= r + r(\cos\theta)^2 - 2R\cos\theta \\ b_3 &= R - r\cos\theta. \end{aligned} \quad (5)$$

Due to the fact that  $R \approx r$ , it follows that  $b_2 \approx r(\cos\theta - 1)^2$ . This relationship holds when  $\theta$  is less than  $45^\circ$ ,  $(\cos\theta - 1)^2 < 0.086$ . Therefore, when  $\theta$  is small,  $(\cos\theta - 1)^2$  can be neglected, and  $m_s^y$  can be simplified as

$$m_s^y = f_s^x(2b_3/\sin\theta - l + \mu r + \mu^2 l) + f_s^z(2\mu b_3/\sin\theta - 2\mu l + \mu^2 r)/(1 + \mu^2). \quad (6)$$

2) *Deviations Estimation:* The friction coefficient between two materials is influenced by various factors, such as temperature, pressure, surface roughness, and shape. Therefore, relying solely on a reference value is not always practical. This article proposes an estimation of the friction coefficient  $\mu^*$  by solving the following optimization problem:

$$\begin{aligned} \mu^* = \arg \min_{\mu} \sum_{i=1}^n & \left\| \hat{m}_{s_i}^y - m_{s_i}^y \right\| \\ \text{s.t. } \hat{m}_{s_i}^y = & f(\mu, f_{s_i}^x, f_{s_i}^z, r, R, l, \theta_i) \end{aligned} \quad (7)$$

where  $\hat{m}_{s\ i}^y$  is calculated according to (4) or (6), and  $l$ ,  $r$ , and  $R$  are known geometric parameters which can be obtained by CAD model or measurement, while  $\theta_i$ ,  $f_{s\ i}^x$ , and  $f_{s\ i}^z$  are measurable by instruments and force/torque sensors. By leveraging the contact forces/torques observed within a period of time under the constrained state and utilizing the estimated friction coefficient  $\mu^*$  derived from (7), it becomes possible to estimate the current angle  $\theta$  in real time. The estimation method is similar to (7), which is

$$\begin{aligned} \hat{\theta} = \arg \min_{\theta} & \sum_{i=1}^n \left\| \hat{m}_{s_i}^y - m_{s_i}^y \right\| \\ \text{s.t. } & \hat{m}_{s_i}^y = f(\mu^*, f_{s_i}^x, f_{s_i}^z, r, R, l, \theta). \end{aligned} \quad (8)$$

The position deviation of the point  $O_p$  to the  $Z_h$  axis in the  $X_h$  direction can be approximated as

$$\hat{\Delta}d = |C_o O_{p'}| \sin \hat{\theta} = R - r \cos \hat{\theta}. \quad (9)$$

According to (8) and (9), the robot will rotate and move the pegs in the air to compensate for the deviations.

#### D. Insertion Under Residual Deviations

Due to various factors, including inherent robot motion errors and the estimation errors of the previous stage's angular deviation  $\theta$ , small residual deviations between the pegs and the holes remain at the beginning of the third stage. However, these residual deviations pose a challenge for achieving high-precision multiple PIH assemblies. Relying solely on compliant control methods like IMC is insufficient to smoothly accomplish the insertion. IL methods are commonly applied for learning skills that involve force-related tasks, offering the advantages of reduced programming burden and the directness and simplicity of acquiring skills from demonstration data [34]. However, previous IL methods typically train a policy in the sparse 12-dimensional force–action space, which presents difficulties in terms of training efficiency and data utilization [35]. To address these issues, this article proposes a method that combines IMC with an IL-based approach.

1) *Skill Learning*: The deviations and contact forces are primarily concentrated within the plane  $X_p O_p Z_p$ . Because the deviations in other dimensions are exceedingly negligible, IMC is capable of effectively eliminating such deviations. The primary source of deviations during the insertion stage arises from the estimation errors of the  $\theta$ , which is also the predominant deviation affecting the insertion process. Therefore, in the proposed approach, the dimensionality of the skill learning space during the insertion stage can be reduced to four dimensions, compared to the previous 12 dimensions in [16], [36], [37]. The mapping function  $f(F_p, \omega_y) : \mathbb{R}^3 \mapsto \mathbb{R}$  can be represented as

$$f(f_p^x, f_p^z, m_p^y, \omega_y) : \{f_p^x, f_p^z, m_p^y\} \mapsto \omega_y \quad (10)$$

where  $\omega_y$  represents the angular velocity in the  $Y_p$  axis direction. The establishment of this mapping solely to  $\omega_y$  is due to the fact that once the angular deviation  $\theta$  is adjusted and eliminated, the jamming phenomenon can be resolved, leading to the successful completion of the insertion. This reduction in dimensions helps to avoid the issues of sparse training space and low efficiency of training and data utilization, allowing the fulfillment of policy training requirements with a small amount of demonstration data.

Insertion skills are demonstrated by human, and GMM is adopted to encode demonstration data as a probabilistic model. For a data point  $\xi = \{\xi^I, \xi^O\} \in \mathbb{R}^4$ , the probability of it belonging to the learned GMM is

$$P(\xi) = \sum_{k=1}^K \pi_k \mathcal{N}(\xi | \mu_k, \Sigma_k) \quad (11)$$

where  $\pi_k \in [0, 1]$ ,  $\mu_k$  and  $\Sigma_k$  are prior probability, center and covariance matrix of the  $k$ -th Gaussian in the GMM. The mapping is obtained by using GMR, which can give a conditional expectation of output  $\xi^O = \omega_y$  for a given input  $\xi^I = \{f_p^x, f_p^z, m_p^y\}$

$$E\{P(\xi^O | \xi^I)\} = E\left\{\sum_{k=1}^K h_k \mathcal{N}(\hat{\xi}_k, \hat{\Sigma}_k)\right\} \quad (12)$$

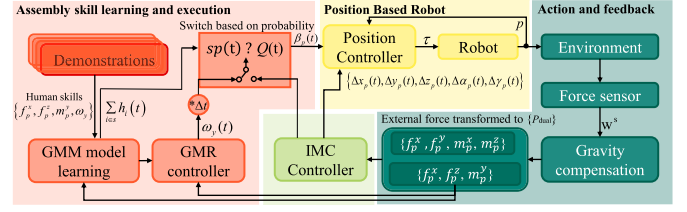


Fig. 5. Control block for the third stage.  $\Delta x_p(t)$ ,  $\Delta y_p(t)$ ,  $\Delta z_p(t)$ ,  $\Delta \alpha_p(t)$ ,  $\Delta \beta_p(t)$ , and  $\Delta \gamma_p(t)$  are the increment of translation and rotation in the  $X_p$ ,  $Y_p$ , and  $Z_p$  directions.

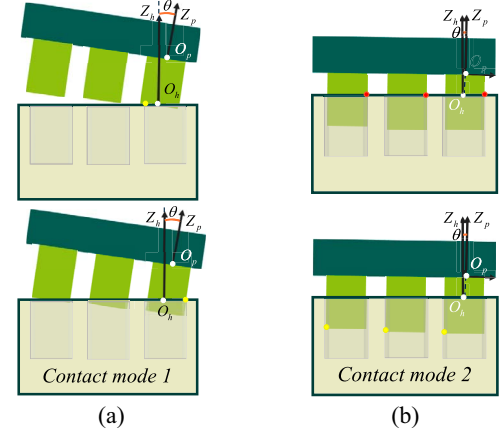


Fig. 6. Two contact modes. (a) Contact mode one. (b) Contact mode two.

where  $h_k$  represents the probability that  $k$ -th Gaussian component is responsible for  $\xi^I$

$$\begin{aligned} h_k &= p(k | \xi^I) = \frac{p(k)p(\xi^I | k)}{\sum_{j=1}^K p(j)p(\xi^I | j)} \\ &= \frac{\pi_k \mathcal{N}(\xi^I; \mu_k^I, \Sigma_k^I)}{\sum_{j=1}^K \pi_j \mathcal{N}(\xi^I; \mu_j^I, \Sigma_j^I)}. \end{aligned} \quad (13)$$

2) *Control Method*: The insertion control strategy is depicted in the control block diagram (Fig. 5). Because the deviations outside of the plane  $X_p O_p Z_p$  are negligible, an IMC with large inertia and damping parameters is set to reduce the responsiveness of translations in the  $Y_p$  directions and rotation around the  $X_p, Z_p$  directions. In the context of motion control within the  $X_p O_p Z_p$  plane, a proportional-derivative (PD) controller is employed specifically for the  $Z_p$  direction to enforce a consistent insertion force, and the IMC is used to maintain the force in the  $X_p$  direction near zero. Moreover, the control methods of the rotation  $\beta_p$  around the  $Y_p$  direction are determined based on two distinct contact modes (as shown in Fig. 6):

- 1) Mode 1: Pegs on one side of the projection plane make contact with the holes, typically associated with a relatively large angular deviation  $\theta$ .
- 2) Mode 2: Pegs at different positions on the projection plane make contact with the holes. This mode often corresponds to a relatively small angular deviation  $\theta$ .

In this study, we will select the more appropriate control method for the  $\beta_p$  between IMC and GMR (12) based on the characteristics of the two contact modes. Contact mode 1 exhibits relatively large resultant forces in the  $X_p$  direction, which is due to the large angular deviation  $\theta$  and a concentration of contact points on one side. Consequently, this mode is prone to jamming. Relying solely on IMC for reducing the  $\theta$  may lead to erroneous adjustments and compromise precision and response speed [26]. In comparison, employing GMR for  $\omega_y$  enables rapid elimination of large angular  $\theta$ . In the context of contact mode 2, it exhibits smaller resultant forces in the  $X_p$  direction and angular velocity in the  $Y_p$  direction. As shown in Fig. 6(b), the contact points are dispersed, and at any given moment, they are either all red or all yellow. Therefore, the contact force in the  $X_p$  direction fluctuates within a small range near zero, resulting in a more limited range of motion for the pegs. These constraints confine the pegs' motion within a narrow range favorable for insertion [33]. Besides, the  $\theta$  is already very small, so the IMC is sufficient for the control of  $\beta_p$  to achieve efficient assembly with stability. However, the control of  $\omega_y$  from GMR is not suitable for mode 2 due to the limited range of motion because the adverse effects resulting from suboptimal demonstration data or sensor errors can result in excessive contact forces or even jamming.

Based on the aforementioned characteristics, this article proposes a rapid insertion control method within the constrained space, as described in Algorithm 1. First, human assembly demonstrations are conducted within the constrained space, and data is collected to learn the GMM model parameters. Based on the different features of contact force/torque and  $\omega_y$  for the two contact modes, the K-means clustering algorithm is then utilized to divide the centers of the Gaussians in the GMM into three groups, each group possessing center points  $\mu^j = \{\mu_{f_x}^j, \mu_{f_z}^j, \mu_{m_y}^j, \mu_{\omega_y}^j\}$ ,  $j = 1, 2$  or  $3$ . The Gaussians that belong to the group with the minimum absolute values for  $\mu_{f_x}^j$  and  $\mu_{\omega_y}^j$  are assigned to set  $S$ , in which the Gaussians correspond to the second contact mode. In the control loop, the probabilities of the current  $\xi^T$  at each step being attributed to all Gaussians in set  $S$  are calculated based on (13), and the probabilities are summed to obtain  $s_p(t)$ . Based on a comparison between the randomly generated number  $Q(t)$  and  $s_p(t)$ , the robot determines whether the current output angular velocity  $\omega_y(t)$  is determined by IMC or calculated according to (12) through GMR. It is worth noting that after the first stage, it is necessary to calculate the current prior probability  $s_p(t)$  based on (13).

### III. EXPERIMENT

This section primarily concerns validation and comparative experiments on the proposed strategy and methods. The experiment system configuration is shown in Fig. 7. The Gamma model ATI force/torque sensor and UR5 robot were selected, and an adjustable-angle locking plier was used to change the orientation of the pegs. A detachable teaching device was created using the ATI sensor, Optitrack marker balls, and a

#### Algorithm 1: Execution of inserting motion.

**Input:**  $\{\pi_k, \mu_k, \Sigma_k\}_{k=1}^K$ , controller cycle  $\Delta t$

- 1 Employ K-means to divide  $\{\mu_k\}_{k=1}^K$  into three groups  $\{\mu_{f_x}^j, \mu_{f_z}^j, \mu_{m_y}^j, \mu_{\omega_y}^j\}_{j=1}^3$
- 2 Label the group with the smallest absolute values for  $\mu_{f_x}^j$  and  $\mu_{\omega_y}^j$  as  $S$
- 3  $t \leftarrow 0$ ;
- 4 **while** *Insert depth*  $< l$  **do**
- 5   Calculate  $\Delta z_p(t)$  according to the PD controller
- 6   Calculate  $\{\Delta x_p(t), \Delta y_p(t), \Delta \alpha_p(t), \Delta \gamma_p(t)\}$  according to the IMC controller
- 7    $\{h_k(t)\}_{k=1}^K \leftarrow$  Probability for Gaussians in  $S$  using (13)
- 8    $sp(t) \leftarrow \sum_{i \in S} h_i(t)$
- 9   Generate  $Q(t) \sim \mathcal{U}(0, 1)$
- 10   **if**  $sp(t) < Q(t)$  **then**
- 11      $\omega_y(t) \leftarrow$  Expectation based on GMR using (12)
- 12      $\Delta \beta_p(t) \leftarrow \omega_y(t) \Delta t$
- 13   **else**
- 14     Calculate  $\Delta \beta_p(t)$  according to the IMC controller
- 15   **endif**
- 16 Execute motion
- 17  $\{\Delta x_p(t), \Delta y_p(t), \Delta z_p(t), \Delta \alpha_p(t), \Delta \beta_p(t), \Delta \gamma_p(t)\}$
- 18 **endwhile**

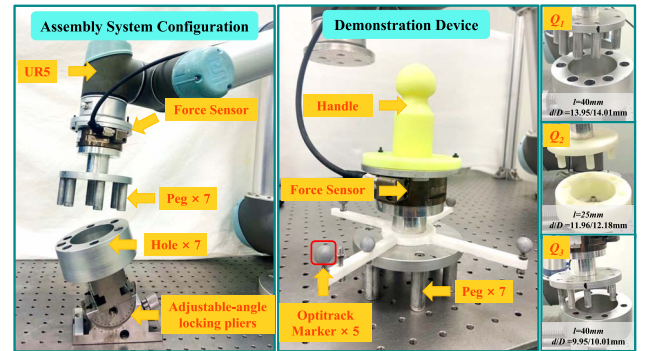


Fig. 7. Experiment system configuration.

3-D-printed handle, allowing humans to complete the teaching process without physically manipulating the robot's end effector. The experiments employed three sets of components, and their respective parameters are presented in Table I. The distribution of the seven pegs and holes for  $Q_1$  and  $Q_3$  on their respective discs exhibits nonuniformity. It is worth mentioning that the selection of the number of pegs and holes, the uneven distribution, and the clearance in the experimental design of this article are quite challenging, which can well demonstrate the effect of proposed method.

TABLE I  
INFORMATION OF PEGS AND HOLES

Label	Material	Number of Pegs	Length	Diameters (d/D)
$Q_1$	Aluminum alloy	7	40 mm	13.95/14.01 mm
$Q_2$	Photosensitive resin	6	25 mm	11.96/12.18 mm
$Q_3$	Aluminum alloy	7	40 mm	9.95/10.01 mm

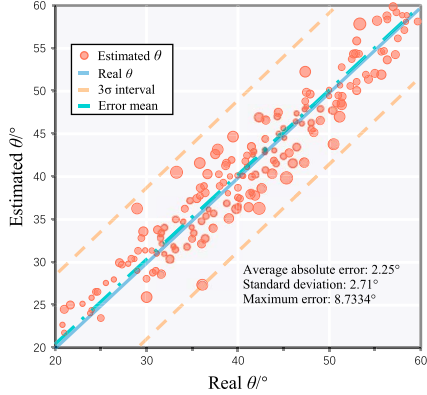


Fig. 8. Estimation of the angle  $\theta$  for  $Q_1$ .

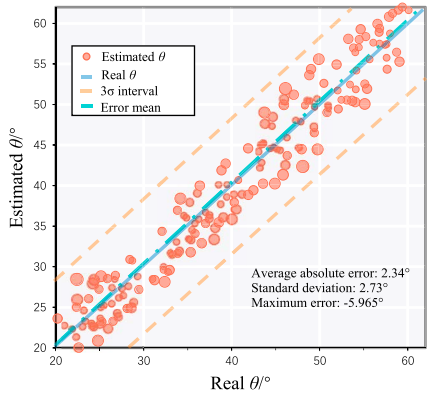


Fig. 9. Estimation of the angle  $\theta$  for  $Q_2$ .

#### A. Verification of Deviation Estimation

In the experiment, the pegs were first controlled to achieve the constrained state, as shown in Fig. 11(a) and 11(b). To estimate the friction coefficient  $\mu$ , 20 sets of contact forces and actual angle information were recorded under different deviations from  $20^\circ$  to  $60^\circ$ . During this process, the two pegs applied forces of 15 N and 5 N in the  $-X_p$  and  $-Z_p$  directions, respectively. SciPy, an open-source software package for mathematics, was utilized to calculate the friction coefficient with an initial value of  $\mu_0 = 0.4$ . Based on (7), the optimal friction coefficients  $\mu^*$  relative to  $Q_1$ ,  $Q_2$ , and  $Q_3$  were calculated as 0.3889, 0.4122, and 0.3947, respectively.

During the deviation estimation phase, the deviations  $\theta$  were randomly set. The estimated deviation angles were calculated using  $\mu^*$  and a period of contact forces according to (8). This

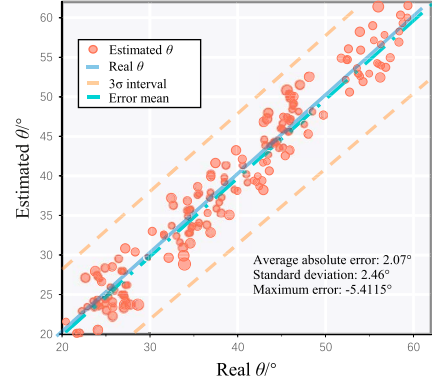


Fig. 10. Estimation of the angle  $\theta$  for  $Q_3$ .

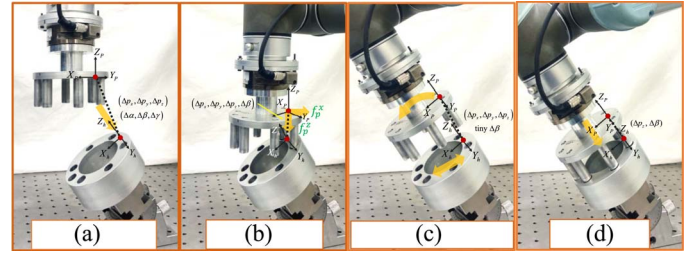


Fig. 11. Process of the multiple PIH strategy. (a) Pegs approaches the holes. (b) Robot adjusts the pegs to contact the holes in the constrained state. (c) The pegs are rotated and translated by the robot to compensate for the estimated deviations. (d) Pegs are moved back to insert into the holes.

process was repeated 180 times for each set of components. The results are presented in Figs. 8–10, where the size of each red point indicates the magnitude of the estimation error, and the region enclosed by the two yellow lines represents the three-standard-deviation interval of the estimation. The deviation estimation results on the three sets of components exhibit minimal differences, with average absolute estimation errors of  $2.25^\circ$ ,  $2.34^\circ$ , and  $2.46^\circ$ , respectively. The maximum estimation error occurs in the  $Q_1$  group, measuring  $8.7334^\circ$ , which exceeds the value of  $\arccos(d/D) = 5.3^\circ$ . However, this residual deviation can still be rapidly eliminated through the proposed insertion control algorithm in the third stage. The above deviation angle estimation errors are significantly smaller compared to the deviations before compensation. Additionally, the residual estimation errors can be rapidly and stably eliminated in the subsequent third stage through the proposed insertion control algorithm. Therefore, these results are acceptable within the strategy proposed in this article. After obtaining the solution for  $\theta$ , the robot lifted the pegs to the free space, where it compensated for the residual  $\theta$  and positional deviations, before moving the pegs back to contact the holes [see Fig. 11(c)].

#### B. Demonstration and Model Learning

Because the constrained state is in a data-compressed space, only a few demonstrations are needed. Additionally, to better



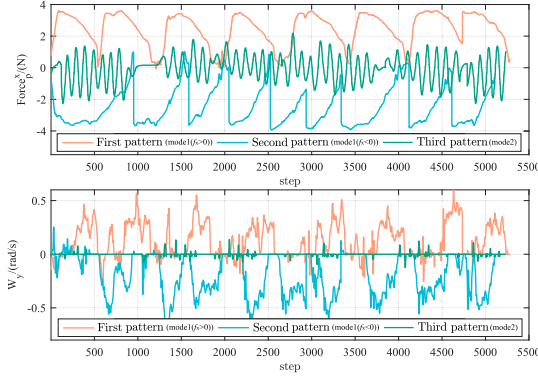


Fig. 12. Demonstration data of  $f_p^x$  and  $w_y$  for the three patterns.

TABLE II  
PARAMETERS OF GAUSSIANS IN THE GMM MODEL FOR  $Q_1$

	$G_1^{Q1}$	$G_2^{Q1}$	$G_3^{Q1}$	$G_4^{Q1}$	$G_5^{Q1}$	$G_6^{Q1}$	$G_7^{Q1}$
Priors	0.135	0.134	0.072	0.06	0.174	0.192	0.234
$\mu_{f_x}$ (N)	3.42	-3.52	-0.702	0.72	2.45	-2.50	0.032
$\mu_{f_z}$ (N)	4.36	5.15	4.66	4.24	4.98	5.50	5.33
$\mu_{m_y}$ (Nm)	-0.12	-0.016	0.11	-0.071	0.033	$-3.7 \times 10^{-3}$	-0.021
$\mu_{\omega_y}$ (rad/s)	$9.4 \times 10^{-3}$	$-8.4 \times 10^{-3}$	0.058	$-1.1 \times 10^{-3}$	0.274	-0.343	$5.1 \times 10^{-5}$

teach and extract the assembly skills, the demonstration actions were divided into three separate patterns. The first two correspond to the contact mode 1 during the insertion stage, with relatively larger initial angular deviations  $\theta$  being positive or negative, respectively. The third pattern is that pegs are compliantly inserted into the holes with relatively smaller initial  $\theta$ , which corresponds to the contact mode 2 during the insertion stage. In these demonstration processes, the constrained state needed to be maintained, which required humans to control the force in the  $Y_h$  and torque in the  $X_h, Z_h$  directions to be as small as possible.

Fig. 12 shows the demonstration data for set  $Q_1$  on  $f_p^x$  and  $\omega_y$  for these three patterns. The  $f_p^x$  and  $\omega_y$  for the first two patterns are relatively higher because of the more pronounced residual angle  $\theta$ . In comparison, it is evident that the third pattern exhibits small forces in the  $X_p$  direction and a low  $\omega_y$  value. The maximum absolute values of  $f_p^x$  and  $\omega_y$  during the demonstration for the third pattern are  $f_{\max}^x = 2.2631$  N and  $\omega_{\max}^y = 0.137$  rad/s, respectively. The contact forces and angular velocity characteristics of the three different contact patterns exhibit consistency across the  $Q_1, Q_2$ , and  $Q_3$  groups. However, their specific features are influenced by factors such as the dimensions of the pegs holes and clearances, resulting in some differences.

The number of Gaussians in the GMM model, denoted by  $\mathcal{K}$ , was seven, which had been determined using the Bayesian information criterion (BIC). The Gaussians corresponding to the set  $S$  were easily determined according to Algorithm 1. For illustrative purposes, this article only provides detailed parameters of the GMM for group  $Q_1$  through Table II. The Gaussians

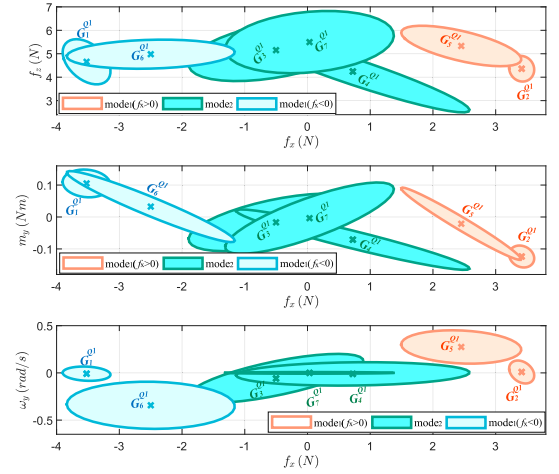


Fig. 13. 2-D presentation of Gaussians for group  $Q_1$ .  $G_3^{Q1}$ ,  $G_4^{Q1}$ , and  $G_7^{Q1}$  belong to the set  $S$ .

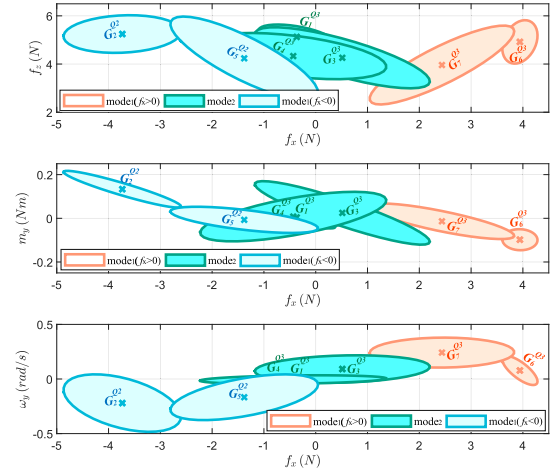


Fig. 14. 2-D presentation of Gaussians for group  $Q_2$ .  $G_1^{Q2}$ ,  $G_3^{Q2}$ , and  $G_4^{Q2}$  belong to the set  $S$ .

labeled as  $G_3^{Q1}$ ,  $G_4^{Q1}$ , and  $G_7^{Q1}$  were assigned to the set  $S$  because the absolute values of  $\mu_{f_x}^j$  and  $\mu_{\omega_y}^j$  of this set were among the smallest, which were 0.0167 N and 0.019 rad/s, respectively. Based on the 2-D visualization of the GMM results for three sets of components in Figs. 13–15, the Gaussians exhibited an overall characteristic of central symmetry. This is due to the fact that in mode 1, the two patterns differ solely in the positive or negative sign of  $\theta$ , resulting in approximate symmetry about the origin in terms of  $f_p^x$ ,  $m_y^y$ , and  $\omega_y$ . While for mode 2, the  $f_p^x$ ,  $m_y^y$ , and  $\omega_y$  are relatively smaller, causing the corresponding Gaussians to concentrate around the origin. This observation aligns with the earlier analysis of the contact modes.

### C. Comparative Evaluation of Insertion Control Method

The proposed insertion control method was compared with four baselines to validate its effectiveness in the presence of small deviations. All of these baselines differed only in the



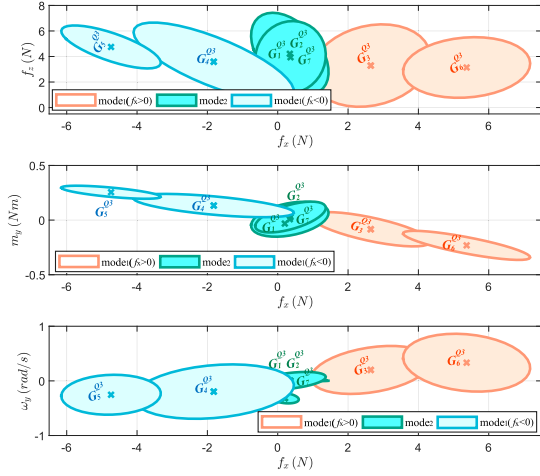


Fig. 15. 2-D presentation of Gaussians for group  $Q_3$ .  $G_1^{Q3}$ ,  $G_2^{Q3}$ , and  $G_3^{Q3}$  belong to the set  $S$ .

control for  $\omega_y$ , while the control for the other motion dimensions was the same as the proposed insertion control method. Method A:  $\omega_y$  is determined by the IMC. Method B: GMR for  $\omega_y = E\{P(\omega_y | \mathbf{F}_p)\}$ . Method C: GMM for  $\omega_y \in P(\omega_y | \mathbf{F}_p)$ . Method D: The control of  $\omega_y$  is alternated between the GMR for  $\omega_y \in E\{P(\omega_y | \mathbf{F}_p)\}$  and IMC at equal frequency. Method E: the proposed method. All experiments started after the second stage. The original angular and pose deviations were set randomly between  $[0^\circ, 10^\circ]$  and  $[-0.5 \text{ mm}, 0.5 \text{ mm}]$ . The desired force in the  $Z_p$  direction was set to 5 N. The evaluation of the methods includes four indexes: success rate (SR), average time cost (ATC), standard deviation of time cost (SDTC), and minimum time cost (MTC), and each method was tested 40 times on each set of components.

As shown in Table III, the use of the IMC controller normally has the lowest success rate and longest time cost because it may lead to misadjustment by oversimplifying the causal relationship between the force/torque and the pose/orientation. Besides, it also cannot get rid of jamming effectively. Method B can complete the insertion task faster with a higher success rate, but it may still cause the pegs to get stuck due to the demanding fitting clearance. Method C can further improve the success rate because it randomly generates  $\omega_y$  which can help get rid of the jamming condition. However, its standard deviation in completion time was higher than that of method B due to the randomness. Because of the larger assembly clearance in the  $Q_2$  group, it exhibits a higher success rate compared to the other two groups, with little difference among the different methods in terms of both average and minimum time costs.

The only difference between E and D is that the switching between the GMR and IMC is not performed at an equal frequency but instead according to the calculated probability  $sp(t)$ . Method D significantly improves the success rate and assembly speed. This is because IMC introduces compliance, which helps improve the instability caused by suboptimal teaching data or sensor errors, such as overly rapid response  $\omega_y$ . Particularly when facing jamming, the switching between different control of  $\omega_y$  introduces disturbances that aid in overcoming the

TABLE III  
RESULT OF THE COMPARATIVE EXPERIMENTS

	Label	A	B	C	D	E
SR	$Q_1$	18/40	29/40	34/40	39/40	40/40
	$Q_2$	22/40	28/40	35/40	40/40	40/40
	$Q_3$	17/40	30/40	32/40	37/40	40/40
ATC(s)	$Q_1$	45.65	30.49	35.38	25.41	19.52
	$Q_2$	20.24	18.44	17.45	17.83	12.56
	$Q_3$	30.47	28.78	26.57	24.90	22.15
SDTC(s)	$Q_1$	8.73	10.45	14.56	11.23	4.46
	$Q_2$	4.30	4.33	6.60	3.50	3.36
	$Q_3$	7.33	4.36	5.44	5.13	3.88
MTC(s)	$Q_1$	28.39	17.51	19.55	15.55	13.54
	$Q_2$	14.89	12.14	10.42	11.40	8.53
	$Q_3$	23.94	19.91	20.67	18.59	18.9

jamming. Proposed method E completed the insertion task with the minimum average time cost while achieving a 100% success rate in all three groups. Moreover, it demonstrated the minimum time cost in the  $Q_1$  and  $Q_2$  groups, with values of 13.54 s and 8.53 s, respectively. However, in the  $Q_3$  group, it showed comparable performance to method D, with a minimum time cost of 18.9 s. Additionally, it exhibited superior performance in terms of the standard deviation of time cost. This reflects that adopting more appropriate control strategies of  $\omega_y$  aiming at different contact modes can significantly enhance the efficiency and stability of the assembly.

#### IV. CONCLUSION

The main contribution of this article is the proposal of a three-stage robotic multiple PIH assembly strategy, along with the deviation estimation method and the fast insertion control method. The proposed strategy involves three successive stages, effectively decomposing the complexity associated with overall analysis and planning control. In the first stage, the deviation is initially constrained within a plane. Subsequently, the second and third stages focus on coarse and fine elimination of the deviations within this plane, respectively. This systematic approach facilitates a step-wise reduction of complexity, enabling precise control and error correction. The deviation estimation method can also be applied in cases where the holes are not horizontal, without the need for visual perception devices. The insertion control algorithm is designed based on the characteristics of different contact modes during the insertion process. It can achieve a 100% success rate and complete the task with a low average time cost in the presence of small residual deviations.

Notably, the current deviation estimation method is based on quasi-static conditions, requiring that we consider the influence of friction forces far greater than the inertia effects of the objects. This necessitates stable contact between the pegs and the holes with minimal occurrence of vibrations. Future work can focus on enhancing contact stability to further improve estimation accuracy.

#### REFERENCES

- [1] F. Guo, Q. Xiao, S. Xiao, and Z. Wang, "Analysis on quantifiable and controllable assembly technology for aeronautical thin-walled structures," *Robot. Comput. Integr. Manuf.*, vol. 80, 2023, Art. no. 102473.

- [2] L. Carlson, H. Huang, N. Alexander, J. Bousquet, M. Farrell, and A. Nikroo, "Automation of nif target fabrication," *Fusion Sci. Technol.*, vol. 70, no. 2, pp. 274–287, 2016.
- [3] A. Manimuthu, V. Venkatesh, Y. Shi, V. R. Sreedharan, and S. L. Koh, "Design and development of automobile assembly model using federated artificial intelligence with smart contract," *Int. J. Prod. Res.*, vol. 60, no. 1, pp. 111–135, 2022.
- [4] J. Song, Q. Chen, and Z. Li, "A peg-in-hole robot assembly system based on Gauss mixture model," *Robot. Comput.-Integr. Manuf.*, vol. 67, 2021, Art. no. 101996.
- [5] J. Xu, C. Zhang, Z. Liu, and Y. Pei, "A review on significant technologies related to the robot-guided intelligent bolt assembly under complex or uncertain working conditions," *IEEE Access*, vol. 7, pp. 136752–136776, 2019.
- [6] L. Jin, Y. Men, R. Song, F. Li, Y. Li, and X. Tian, "Robot skill generalization: Feature-selected adaptation transfer for peg-in-hole assembly," *IEEE Trans. Ind. Electron.*, vol. 71, no. 3, pp. 2748–2757, Mar. 2024.
- [7] Y. Jiang, Z. Huang, B. Yang, and W. Yang, "A review of robotic assembly strategies for the full operation procedure: Planning, execution and evaluation," *Robot. Comput.-Integr. Manuf.*, vol. 78, 2022, Art. no. 102366.
- [8] F. Qin, D. Xu, D. Zhang, and Y. Li, "Robotic skill learning for precision assembly with microscopic vision and force feedback," *IEEE/ASME Trans. Mechatron.*, vol. 24, no. 3, pp. 1117–1128, Jun. 2019.
- [9] T. Jiang, H. Cui, X. Cheng, and W. Tian, "A measurement method for robot peg-in-hole prealignment based on combined two-level visual sensors," *IEEE Trans. Instrum. Meas.*, vol. 70, pp. 1–12, 2020.
- [10] H. Qiao, M. Wang, J. Su, S. Jia, and R. Li, "The concept of "attractive region in environment" and its application in high-precision tasks with low-precision systems," *IEEE/ASME Trans. Mechatron.*, vol. 20, no. 5, pp. 2311–2327, Oct. 2015.
- [11] T. Tang, H.-C. Lin, Y. Zhao, W. Chen, and M. Tomizuka, "Autonomous alignment of peg and hole by force/torque measurement for robotic assembly," in *Proc. IEEE Int. Conf. Automat. Sci. Eng. (CASE)*, Piscataway, NJ, USA: IEEE Press, 2016, pp. 162–167.
- [12] K. Zhang, J. Xu, H. Chen, J. Zhao, and K. Chen, "Jamming analysis and force control for flexible dual peg-in-hole assembly," *IEEE Trans. Ind. Electron.*, vol. 66, no. 3, pp. 1930–1939, Mar. 2019.
- [13] N. Liu, X. Zhou, Z. Liu, H. Wang, and L. Cui, "Learning peg-in-hole assembly using Cartesian DMPS with feedback mechanism," *Assem. Automat.*, vol. 40, no. 6, pp. 895–904, 2020.
- [14] J. Su, Y. Meng, L. Wang, and X. Yang, "Learning to assemble noncylindrical parts using trajectory learning and force tracking," *IEEE/ASME Trans. Mechatron.*, vol. 27, no. 5, pp. 3132–3143, Oct. 2022.
- [15] H. Zhao, Y. Chen, X. Li, and H. Ding, "Robotic peg-in-hole assembly based on reversible dynamic movement primitives and trajectory optimization," *Mechatronics*, vol. 95, 2023, Art. no. 103054.
- [16] X. Gao et al., "Learning force-relevant skills from human demonstration," *Complexity*, vol. 2019, pp. 1–11, Feb. 2019.
- [17] L. Roveda, M. Magni, M. Cantoni, D. Piga, and G. Bucca, "Assembly task learning and optimization through human's demonstration and machine learning," in *Proc. IEEE Int. Conf. Syst., Man, Cybern. (SMC)*, Piscataway, NJ, USA: IEEE Press, 2020, pp. 1852–1859.
- [18] P. Baisong, Y. Tianye, H. Xinda, L. Luping, and W. Weini, "Peg-in-hole assembly strategy based on geometric constraint and hidden Markov model," *Comput. Integr. Manuf. System*, vol. 28, no. 12, 2022, Art. no. 3768.
- [19] Z. Hou, H. Dong, K. Zhang, Q. Gao, K. Chen, and J. Xu, "Knowledge-driven deep deterministic policy gradient for robotic multiple peg-in-hole assembly tasks," in *Proc. IEEE Int. Conf. Robot. Biomimetics (ROBIO)*, Piscataway, NJ, USA: IEEE Press, 2018, pp. 256–261.
- [20] J. Xu, Z. Hou, W. Wang, B. Xu, K. Zhang, and K. Chen, "Feedback deep deterministic policy gradient with fuzzy reward for robotic multiple peg-in-hole assembly tasks," *IEEE Trans. Ind. Inform.*, vol. 15, no. 3, pp. 1658–1667, Mar. 2019.
- [21] F. Shen, Z. Zhang, D. Xu, J. Zhang, and W. Wu, "An automatic assembly control method for peg and hole based on multidimensional micro forces and torques," *Int. J. Precis. Eng. Manuf.*, vol. 20, pp. 1333–1346, May 2019.
- [22] R. Li and H. Qiao, "A survey of methods and strategies for high-precision robotic grasping and assembly tasks—Some new trends," *IEEE/ASME Trans. Mechatron.*, vol. 24, no. 6, pp. 2718–2732, Dec. 2019.
- [23] B. Zhou, L. Liu, and G. Chen, "Contact analysis for dual peg-in-hole assembly of automobile alternator frame," *Mech. Ind.*, vol. 21, no. 2, 2020, Art. no. 209.
- [24] K. Sathirakul and R. H. Sturges, "Jamming conditions for multiple peg-in-hole assemblies," *Robotica*, vol. 16, no. 3, pp. 329–345, 1998.
- [25] S. Yan, D. Xu, and X. Tao, "Hierarchical policy learning with demonstration learning for robotic multiple peg-in-hole assembly tasks," *IEEE Trans. Ind. Inform.*, vol. 19, no. 10, pp. 10254–10264, Oct. 2023.
- [26] Y. Gai, J. Guo, D. Wu, and K. Chen, "Feature-based compliance control for precise peg-in-hole assembly," *IEEE Trans. Ind. Electron.*, vol. 69, no. 9, pp. 9309–9319, Sep. 2022.
- [27] X. Zhao, S. Han, B. Tao, Z. Yin, and H. Ding, "Model-based actor-critic learning of robotic impedance control in complex interactive environment," *IEEE Trans. Ind. Electron.*, vol. 69, no. 12, pp. 13225–13235, 2021.
- [28] S. Lee, "Development of a new variable remote center compliance (VRCC) with modified elastomer shear pad (ESP) for robot assembly," *IEEE Trans. Automat. Sci. Eng.*, vol. 2, no. 2, pp. 193–197, Apr. 2005.
- [29] G. He, S. Shi, D. Wang, and H. Liu, "A strategy for large workpiece assembly based on hybrid impedance control," in *Proc. IEEE Int. Conf. Mechatron. Automat. (ICMA)*, Piscataway, NJ, USA: IEEE Press, 2019, pp. 799–804.
- [30] D. Li, H. Zhao, D. Ge, X. Li, and H. Ding, "A novel robotic multiple peg-in-hole assembly pipeline: Modeling, strategy, and control," *IEEE/ASME Trans. Mechatron.*, early access, Dec. 14, 2023.
- [31] W. Zhang, R. Wang, L. Ji, R. Cao, and L. Chen, "High precise position method based on 2 CCD cameras in alternate-angle image acquisition mode," in *Proc. IEEE Int. Conf. Mechatron., Robot. Automat. (ICMRA)*, Piscataway, NJ, USA: IEEE Press, 2018, pp. 90–94.
- [32] D. Li and X. Pan, "Global calibration of two cameras with optical filter with non-overlapping views using 1D square serrated target," in *Proc. IEEE 3rd Optoelectron. Global Conf. (OGC)*, Piscataway, NJ, USA: IEEE Press, 2018, pp. 76–80.
- [33] K. Zhang, M. Shi, J. Xu, F. Liu, and K. Chen, "Force control for a rigid dual peg-in-hole assembly," *Assem. Automat.*, vol. 37, no. 2, pp. 200–207, 2017.
- [34] H.-I. Lin, "Design of an intelligent robotic precise assembly system for rapid teaching and admittance control," *Robot. Comput.-Integr. Manuf.*, vol. 64, 2020, Art. no. 101946.
- [35] T. Tang, H.-C. Lin, and M. Tomizuka, "A learning-based framework for robot peg-hole-insertion," in *Proc. Dyn. Syst. Control Conf.*, vol. 57250, Columbus, Ohio, USA: ASME, 2015, p. V002T27A002.
- [36] T. Tang, H.-C. Lin, Y. Zhao, Y. Fan, W. Chen, and M. Tomizuka, "Teach industrial robots peg-hole-insertion by human demonstration," in *Proc. IEEE Int. Conf. Adv. Intell. Mechatron. (AIM)*, Piscataway, NJ, USA: IEEE Press, 2016, pp. 488–494.
- [37] P. Wang, J. Zhu, W. Feng, and Y. Ou, "Robot learning from human demonstration of peg-in-hole task," in *Proc. IEEE 8th Annu. Int. Conf. CYBER Technol. Automat., Control, Intell. Syst. (CYBER)*, Piscataway, NJ, USA: IEEE Press, 2018, pp. 318–322.

**Dianxi Li** received the B.E. degree in mechanical engineering in 2021 from the School of Mechanical Science and Engineering, Huazhong University of Science and Technology, Wuhan, China, where he is currently working toward the M.E. degree in mechatronic engineering.

His research interests include imitation learning and robotic assembly.



**Xiangfei Li** (Member, IEEE) received the B.E. degree in mechanical engineering and automation from the School of Mechanical Science and Engineering, Jilin University, Changchun, China, in 2012, and the Ph.D. degree in mechatronics engineering from the School of Mechanical Science and Engineering, Huazhong University of Science and Technology, Wuhan, China, in 2020.



He is currently a Postdoctoral Researcher with Huazhong University of Science and Technology. His research interests include visual servoing, skills learning, and motion control.



**Huan Zhao** (Member, IEEE) received the B.E. degree in mechanical engineering and automation from the School of Mechanical Science and Engineering, Jilin University, Changchun, China, in 2006, and the Ph.D. degree in mechatronics engineering from the School of Mechanical Engineering, Shanghai Jiao Tong University, Shanghai, China, in 2013.

From 2013 to 2015, he was a Postdoctoral Researcher with Huazhong University of Science and Technology, Wuhan, China. Since 2015, he has been with Huazhong University of Science and Technology, where he is currently a Professor. His research interests include robotic machining and assembly.



**Dongsheng Ge** received the B.E. degree in mechanical engineering from the School of Mechanical Engineering, Hefei University of Technology, Hefei, China, in 2017, and the M.E. degree in mechanical engineering in 2020 from School of Mechanical Science and Engineering (MSE), Huazhong University of Science and Technology (HUST), Wuhan, China, where he is currently working toward the Ph.D. degree.

His research interests include robot control, learning, and multirobot collaboration.



**Han Ding** (Senior Member, IEEE) received the Ph.D. degree in mechanical engineering from Huazhong University of Science and Technology (HUST), Wuhan, China, in 1989.

He was supported by the Alexander von Humboldt Foundation when he was with the University of Stuttgart, Stuttgart, Germany, from 1993 to 1994. Since 1997, he has been a Professor with HUST, where he is currently the Dean of the Future Institute of Technology. He was a Cheung Kong Chair Professor with Shanghai Jiao Tong University, Shanghai, China, from 2001 to 2006. He was elected a member of the Chinese Academy of Sciences in 2013. His research interests include robotics, control engineering, and digital manufacturing.

Dr. Ding is also an Editor of IEEE TRANSACTIONS ON AUTOMATION SCIENCE AND ENGINEERING and a Senior Editor of IEEE ROBOTICS AND AUTOMATION LETTERS.